Manuscript prepared for The Cryosphere
with version 4.2 of the LaTeX class copernicus.cls.
Date: 30 September 2013

Updated cloud physics improve the modelled near-surface climate of Antarctica of a regional atmospheric climate model

J. M. van Wessem[1], C. H. Reijmer[1], J. T. M. Lenaerts[1], W. J. van de Berg[1], M. R. van den Broeke[1], and E. van Meijgaard[2]

[1]Institute for Marine and Atmospheric Research Utrecht, Utrecht University, Utrecht, the Netherlands
[2]Royal Netherlands Meteorological Institute, De Bilt, the Netherlands

Correspondence to: J. M. van Wessem (j.m.vanwessem@uu.nl)

Abstract. The physics package of the polar version of the regional atmospheric climate model RACMO2 has been updated from RACMO2.1 to RACMO2.3. The update primarily consists of an improved turbulent and radiative flux scheme and a changed cloud scheme that includes a parameterization for ice cloud super-saturation. In this study the effects of these changes on the modelled surface energy balance, near-surface temperature and wind speed of Antarctica are presented. The ice cloud super-saturation has led to more moisture being transported onto the continent, resulting in more and optically thicker clouds and more downward longwave radiation. As a result, overall RACMO2.3 better represents the near-surface climate in terms of the modelled surface energy balance, based on a comparison with > 750 months of data from nine automatic weather stations located in East Antarctica. Especially the representation of the sensible heat flux and net longwave radiative flux has improved with a decrease in biases of up to 40 %. As a result, modelled surface temperatures have increased and the bias, when compared to 10 m snow temperatures from 64 ice core observations, has decreased from -2.3 K to -1.3 K. The weaker surface temperature inversion consequently improves the representation of the sensible heat flux, whereas wind speed remains unchanged. However, significant model biases remain, partly because RACMO2 at a resolution of 27 km is unable to resolve steep topography.

1 Introduction

Regional atmospheric climate models (RCMs) are important tools to improve our understanding of atmospheric processes and their relation to climate change. They provide a physically coherent representation of the climate in areas with a low spatial and temporal coverage of observations. RCMs

are also capable of resolving detailed features that are not captured by global circulation models (GCMs). Specifically, RCMs have been successfully applied to remote areas such as Antarctica (e.g. Van Lipzig et al., 2002) and Greenland (Fettweis, 2007; Ettema et al., 2010a) to assess the climate and surface mass balance of the ice sheet (e.g. Van de Berg et al., 2005; Lenaerts et al., 2012). Moreover, the RCM output can be used to enhance the interpretation of remote sensing data such as GRACE (Chen et al., 2006) and InSAR (Rignot et al., 2008). In combination with a firn densification model, RCM output provides a correction for firn densification in support of radar/laser altimetry (Ligtenberg et al., 2012). All techniques combined have recently provided a synthesis of mass balance estimates for the Greenland and Antarctic ice sheets (Shepherd et al., 2012).

The Regional Atmospheric Climate Model RACMO2, which has been adapted for specific use over the polar regions, has recently undergone a major update of its physics package. In the present study we show whether this update from version RACMO2.1 to RACMO2.3 has improved the representation of the Antarctic climate, with its extreme temperatures and winds. Even though RACMO2.1 has proved to realistically simulate the Antarctic near-surface climate (Van de Berg et al., 2005; Lenaerts et al., 2012), previous model evaluations showed that downward longwave radiation is generally underestimated by the model (Van de Berg et al., 2007) resulting in a significant cold surface bias (Van den Broeke, 2008). To see whether this has improved in RACMO2.3 we will assess the changes for Antarctica in the modelled surface energy balance (SEB), near-surface wind speeds and surface temperatures and compare these to available observations. Section 2 discusses the model, the changes in model formulation and the observational data used for evaluation. In Sect. 3 the effects of the model changes on clouds, the SEB and the near-surface temperature and wind are presented and a comparison is made to observational data (Sect. 3.3 – 3.5), followed by conclusions in Sect. 4.

2 Data and methods

2.1 RACMO2 physics update

RACMO2 combines the dynamical processes of the High Resolution Limited Area Model (HIRLAM) (Undén et al., 2002) with the physics package of the European Centre for Medium-range Weather Forecasts (ECMWF) Integrated Forecast System (IFS). RACMO2 has been specifically adapted for use over the large ice sheets of Greenland and Antarctica (e.g. Reijmer et al., 2005). It is interactively coupled to a multilayer snow model that calculates melt, percolation, refreezing and runoff of meltwater (Ettema et al., 2010b; Greuell and Konzelmann, 1994). Surface albedo is based on a prognostic scheme for snow grain size (Kuipers Munneke et al., 2011) and a drifting snow routine simulates the interactions of drifting snow with the surface and the lower atmosphere (Lenaerts et al., 2012). A horizontal resolution of $\sim$27 km and a vertical resolution of 40 levels is used. The model is forced by ERA-Interim re-analysis data (January 1979–December 2011, Dee et al., 2011) at the

ocean and lateral boundaries, while the domain interior is allowed to evolve freely.

Here we analyse changes in the modelled Antarctic near-surface climate after the ECMWF IFS physics package cycle CY23r4 in RACMO2.1 (White, 2001) has been updated to cycle CY33r1 in RACMO2.3 (ECWMF-IFS, 2008). The updates that have the most impact on Antarctic applications are the changes in the cloud scheme, the cloud microphysics and the radiation and turbulence schemes. All changes will be described below and are discussed in more detail in relation with the results in Sect. 3.5.

An important change in the cloud scheme is the inclusion of a parameterization for ice supersaturation as described by Tompkins and Gierens (2007). As a result, the specific humidity of cold air parcels (at temperatures where the difference between liquid water and ice saturation pressure is large) has to reach a higher value in order for condensation to occur. This leads to an improved representation of clouds and moisture concentrations in the (upper) troposphere (Tompkins and Gierens, 2007). Aircraft observations with the Microwave Limb Sounder (MLS) have shown that supersaturation frequently occurs over the steep coastal regions of Antarctica (Spichtinger et al., 2003). Simulations with the ECMWF IFS have already shown that the new parameterization leads to a better global distribution of super-saturated atmospheres, albeit a slight underestimation for Antarctica remains (Tompkins and Gierens, 2007).

Another change in the physics is the introduction of the McRad radiation scheme (Morcrette et al., 2008). It describes short- and longwave radiation transfer through clouds, based on the Monte Carlo Independent Column Approximation (McICA, Barker et al., 2008), and a revision of cloud optical properties making the parameterizations that use these properties more accurate. This improves the interaction of multi-layer cloud cover with short- and longwave radiation, but is believed to be of minor importance for Antarctica, considering the low occurrence frequency of these cloud types in this region. In the shortwave radiation scheme (SRTM, Mlawer and Clough, 1997) the Fouqart-Bonnel scheme is replaced by a scheme that is based on the correlated k-method (Lacis, 1991). The latter is shown to lead to an overall improved accuracy in calculated fluxes and heating rates (ECWMF-IFS, 2008).

The last relevant physics change is the newly implemented Eddy-Diffusivity Mass Flux (EDMF, Siebesma et al., 2007) scheme for boundary-layer turbulence/shallow convection. This scheme distinguishes between large-scale (updraughts) and small-scale (turbulence) mixing processes in the surface and boundary layer by describing them with either mass fluxes or diffusion. The surface flux relies on Monin-Obukhov similarity theory but takes into account form drag (Beljaars et al., 2004) that is dependent on subscale orography. For topographically rough areas like the Antarctic Peninsula these changes are expected to be especially important.

There are other minor changes in the model but these are of little significance in the context of this study. For instance the RACMO2 model update also incorporates changes in the HIRLAM dynamical core. These are mostly of numerical nature and are not addressed here. For a more detailed

and complete description of the entire RACMO2 update the reader is referred to Van Meijgaard et al. (2012) and ECWMF-IFS (2008) and references therein.

2.2 Observational data

The near-surface wind, temperature and SEB are evaluated using observational data from nine automatic weather stations (AWS). These AWSs were selected because they measure all four radiation components as well as humidity, and therefore enable a reliable closure of the SEB. Figure 1 shows the locations of the AWSs. They are located in different climate regimes: from relatively mild and wet coastal sites (AWS 4 and 11) to the steep escarpment region of Dronning Maud Land (DML) (AWS 5, 6 and 16), the South Dome of Berkner Island (AWS 10) and the high and cold East Antarctic plateau (AWS 8, 9 and 12). Due to instrumental problems and icing of the sensors some months of the data are of lower quality. Observation lengths range from 4 to 15 yr of data. A summary of the location and data records of the AWSs is provided in Table 1. All AWSs are of similar design: single level measurements of wind speed/direction, temperature and relative humidity are performed at a height of approximately 3 m. The individual radiation components (SW↓, SW↑, LW↓, LW↑) are measured with a single sensor. For more details see Van den Broeke et al. (2005a,b) and Reijmer and Oerlemans (2002).

The SEB can be written as:

$$M = SW_{net} + LW_{net} + SHF + LHF + G, \quad (1)$$

where fluxes directed towards the surface are defined positive with units W m^{-2}, M is melt energy ($M = 0$ if the surface temperature $T_{\mathrm{s}} < 273.15$ K), SW_{net} and LW_{net} are the net shortwave and longwave radiative fluxes, SHF and LHF are the sensible and latent heat fluxes and G is the subsurface conductive heat flux. The sensible- and latent heat fluxes are calculated using Monin-Obukhov similarity theory using the bulk method (Van den Broeke et al., 2005b). Treatment of the radiation fluxes is as in Van den Broeke (2004). All data from the nine AWSs are monthly averaged (resulting in 770 months) and compared with data from the same months of the two RACMO cycles. An assessment of the quality of the observational data can be found in Reijmer and Oerlemans (2002); Van den Broeke et al. (2004). Note that the above implies that the turbulent fluxes and surface temperatures are calculated values and not direct measurements.

As the AWSs only cover a limited part of East Antarctica, 64 snow temperature observations (Fig. 1) are additionally used to evaluate the spatial performance of RACMO2 for T_{s}. The modelled surface temperature, averaged over 1979 to 2011, is compared to snow temperature measurements at 10 m depth similar to Van de Berg et al. (2007). The 10 m snow temperature is assumed to be representative for the annual mean surface temperature. Note that at 27 km, the observational data are compared with data from the nearest model grid point. For the 10 m snow temperatures, this causes four locations to fall outside of the ice mask. For these points the nearest grid point that does fall within the ice mask is used.

3 Results

3.1 General climate characteristics

In Antarctica a negative to zero net radiation budget prevails year round. In summer the radiation budget regularly becomes positive due to absorption of shortwave radiation at the surface. In winter, the radiation budget is balanced mainly by a positive (downward directed) SHF, as LHF is generally small due to the low humidity and thus small near-surface moisture gradients exist over the Antarctic Ice Sheet (AIS). The negative radiation budget prevails and cools the surface, resulting in a quasi-permanent surface-based temperature inversion. In combination with a sloping surface, this leads to the characteristic persistent katabatic winds over the AIS. As the cooling is stronger in winter, the katabatic winds increase in strength in winter. Stronger katabatic winds enhance downward sensible heat transport, which counteracts the strength of the surface temperature inversion by increasing the surface temperature. This results in a weaker seasonality of (near) surface temperature in high wind speed areas.

To illustrate these interactive processes, Fig. 2 shows the monthly mean values of 10 m wind speed (V_{10m}), surface temperature ($T_{\rm s}$), net longwave radiation (LW_{net}) and sensible heat flux (SHF) for four AWSs in different climate zones of the AIS (4, 5, 6 and 9). Figure 2a shows that monthly mean wind speeds for AWS 5 and 6, in the steep escarpment region, exhibit a strong seasonal cycle due to stronger katabatic forcing in winter, with monthly wind speeds up to 9 m s^{-1}. These katabatic winds mix warm air downward to the surface (large SHF), increasing surface temperature (Fig. 2b), and hence upward longwave radiation (Fig. 2c). For AWS 4 and AWS 9, located on the relatively flat coastal ice shelf and interior ice sheet, respectively, wind speeds are lower, weak (AWS 4) and non-katabatic (AWS 9) and show no seasonal cycle. At these sites the seasonal amplitude in temperature is larger than at the sites dominated by katabatic winds (AWS 5 and 6) mainly because the wintertime surface temperature inversion is stronger.

3.2 Changes in cloud properties and impact on simulated near-surface variables

The new parameterization for cloud ice super-saturation, included in the new RACMO2 physics cycle, changes the total amount of modelled clouds over Antarctica, most notably over the East Antarctic plateau. To illustrate this effect, Fig. 3 shows a latitudinal cross-section of the vertical distribution of total cloud water/ice content, averaged over the period 2007–2010 (representative for the entire simulation). A significant increase of modelled cloud content is found over the East Antarctic plateau, while cloud content has decreased along the coastline and over the ocean. With the new parameterization, moist air that reaches the continent has to exceed 100% relative humidity up to 150% in order to form clouds. As a result, clouds form further inland and higher up in the troposphere, resulting in more clouds simulated by RACMO2.3 in the interior.

The increase in clouds has caused more downward longwave radiation to be emitted as seen in

Fig. 4a, where the difference fields (RACMO2.3 − RACMO2.1) for LW↓, T_s, V_{10m} and SHF are shown. The increase in LW↓ is found on most of the AIS, but is strongest on the East Antarctic plateau, and has led to higher surface temperatures (Fig. 4b), reducing the temperature gradients in the surface layer and resulting in lower SHF values (Fig. 4d). A related pattern in near-surface wind speed is not seen (Fig. 4c), with changes being smaller than 5%.

3.3 Impact on simulation of the Surface Energy Balance

Figure 5 shows the difference of the monthly averaged modelled and observed SEB fluxes for all nine AWSs (>750 months) for RACMO2.3 and RACMO2.1. The average bias and correlation coefficients are summarized in Table 2, as well as the bias standard deviation σ_{bias} and root-mean-square deviation $RMSD$. Most biases (and $RMSD$) are reduced in RACMO2.3: for SHF from 10.5 $\mathrm{W m^{-2}}$ to 7.1 $\mathrm{W m^{-2}}$, for LW_{net} from $-10.4\,\mathrm{W m^{-2}}$ to $-6.3\,\mathrm{W m^{-2}}$. The changes in LHF and SW_{net} are small. For SW_{net} the bias increased from $-1.3\,\mathrm{W m^{-2}}$ to $-2.0\,\mathrm{W m^{-2}}$ but the correlation remains high ($r^2 \simeq 0.93$, with significance level $p < 0.0001$). For LHF the slight improvement from 0.6 $\mathrm{W m^{-2}}$ to 0.4 $\mathrm{W m^{-2}}$ is of little significance due to its small magnitude and the uncertainty of the observed fluxes. The standard deviation σ_{bias} has the same order of magnitude as the bias, suggesting that the improvements are not statistically significant because of the significant noise.

To investigate the seasonal effects, Figure 6 shows the monthly mean difference of SEB fluxes, LW↓ and SW↓ for AWS 4, 5, 6 and 9. LW_{net} is underestimated at the four AWS locations, and most significantly at AWS 4 and 9. The overestimated slope at these two sites is responsible for activating a katabatic feedback in winter, resulting in overestimated SHF. In RACMO2.3, the improved LW↓ reduces this problem for the stations located more inland, as can be seen in Figure 6, most significantly for AWS 9. For AWS 4 the improvement is not related to the increased LW↓, but to a decreased LW↑ (not shown). For this coastal site, V_{10m} that was overestimated has slightly decreased (the performance of the near-surface wind speed will be discussed in Sec. 3.4), resulting in a lower T_s and less longwave cooling. The difference in SW↓ has increased, most notably for the coastal AWSs where changes in cloud content are small. Here, changes in the radiation scheme have led to increased atmospheric transmissivity. For the more inland AWSs the effect is increasingly balanced by increased snowfall, raising the surface albedo and SW↑ (not shown).

The underestimated surface slope results in too low wind speeds at AWS 5 and 6, resulting in an overestimation of the surface temperature inversion (Fig. 8d). As a result, SHF is reasonably well represented, because stability effects remain small even at the underestimated wind speeds (Van den Broeke et al., 2005b). The problem is further reduced in RACMO2.3, in which the SEB at AWS 5 and 6 is well represented.

In summer the SHF bias at AWS 4 is smaller because SW_{net} and LHF help to balance the excess longwave cooling. For AWS 9 however, there is an increased negative bias in SW_{net} in RACMO2.3

due to an overestimated albedo (Van de Berg et al., 2007). To conclude, for most of the climate zones of the AIS the improved representation of SEB components is induced by a better representation of LW↓, but also changes in the turbulence scheme (section 3.5) and small local changes contribute to the improvement.

Figure 5a confirms that high wintertime SHF values in the escarpment zone are well represented, and that RACMO2 generally overestimates SHF in flatter areas. This leads to overestimated T_{s} and hence too negative LW_{net} (Fig. 5d). Both biases are significantly reduced in RACMO2.3, by 33 % (SHF) and 39 % (LW_{net}) respectively. In summer, RACMO2 underestimates SW_{net} in the high interior (Figs. 5c and 6d). As a result of the underestimation of SW_{net}, T_{s} is underestimated (Figs. 7c, d and 8c), the surface temperature inversion overestimated as well as SHF (Figs. 5a, 6d). As a result of too low T_{s}, sublimation (negative LHF) is underestimated and summertime convection (upward SHF) is not modelled on the ice sheet.

3.4 Impact on simulation of temperature and near-surface wind speed

Figure 7 shows modelled values (Fig. 7a, c) and difference (model–observation) (Fig. 7b, d) of the monthly averaged wind speed and surface temperature of all AWSs as a function of the observed value. The figure also shows correlation coefficient r^2 and average bias b, also denoted in Table 2. Figure 7a, b shows that the wind speed representation has not improved in RACMO2.3 when compared to RACMO2.1 (for both datasets: $bias \simeq 0.5$, $r^2 \simeq 0.27$, $p < 0.0001$). Both model cycles generally underestimate high wind speeds and overestimate low wind speeds. Since near-surface winds over the AIS are dominated by katabatic forcing, this is caused by an overestimation of surface slopes in relatively flat areas (AWS 4, 8, 9, 10, 12) and an underestimation of surface slopes in steep areas (AWS 5, 6, 11) owing to the steep terrain of the escarpment region in DML, in combination with the limited horizontal resolution of the model (Reijmer et al., 2005). The small differences in V_{10m} are due to the combined effect of model changes but the errors in wind speed with respect to the observations are dominated by the model topography (note that the model topography is the same in both model cycles).

Figure 8a shows the monthly mean difference (model − observation) of V_{10m} for AWS 4, 5, 6 and 9 respectively. For AWS 5 and AWS 6 (slope $> 10\,\mathrm{m\,km^{-1}}$) wind speed is underestimated year round. For AWS 4 and AWS 9 the wind speed is overestimated in winter, when katabatic forcing is overestimated, and therefore shows a seasonality that is too pronounced. This has a strong effect on the temperature, as shown in Fig. 8b,c, where temperature is underestimated at AWS 5 and 6. The surface temperature inversion, defined here as $T_{inv} = T_{2m} - T_{\mathrm{s}}$, is underestimated when wind speed is overestimated (AWS 4 and 9) (Fig. 8d), which is intuitively expected.

In contrast to wind speed, a clear improvement in surface temperature T_{s} (Fig. 7c, d) in RACMO2.3 over RACMO2.1 is seen, due to the increased LW↓, where the cold bias has been reduced from 3.2 K to 1.9 K while the correlation has not changed ($r^2 = 0.91$, $p < 0.0001$). This improvement occurs

year-round for all the AWSs except for the coastal AWSs (see AWS 4), where the representation was already good due in part to the overestimated wind speed. A comparison of monthly averaged V_{10m} and T_{2m} from the Reference Antarctic Data for Environmental Research (READER, Turner et al., 2004) AWS and surface station data showed similar results and will not be discussed in this study.

Since the AWS are located mainly in DML, which has a topography that is not typical for the entire ice sheet, we use 10 m snow temperature data to obtain a better spatial coverage for the T_{s} evaluation (Fig. 1). Figure 9 shows the difference between modelled and observed T_{s} as a function of the latter, averaged over the model timespan. Average values, bias, σ_{bias}, $RMSD$ and correlation are given in Table 2. Surface temperatures in RACMO2.1 are underestimated at almost all locations and on average are too low by 2.3 K. RACMO2.3 reduces this bias to -1.3 K. Overall the spatial variability of surface temperatures is well represented by both model versions ($r^2 = 0.96$ for RACMO2.1 and $r^2 = 0.98$ for RACMO2.3, $p < 0.0001$) although there seems to be a tendency towards larger underestimations at higher temperature locations. Figure 9 shows that the best agreement is found on the cold East Antarctic plateau, where the overestimated wind speeds compensate the bias in temperature caused by the underestimated LW$\downarrow$. Because of the improved LW$\downarrow$, T_{s} on the plateau has changed from being slightly underestimated in RACMO2.1 to being slightly overestimated in RACMO2.3. In coastal and West Antarctica, T_{s} is underestimated the most, due to both V_{10m} and LW_{net} being underestimated, and it is here that RACMO2.3 produces the largest improvement.

3.5 Impact on SHF regimes

To assess the impact of changes in the atmospheric surface layer scheme Figure 10 shows monthly averaged SHF for all AWSs, RACMO2.3 and RACMO2.1 as a function of the surface temperature inversion and wind speed (color scheme). The filled circles represent winter conditions (April–September), open circles conditions for October–March. Figure 10a clearly shows four regimes. Regime I represents the katabatic wind zone where SHF increases quadratically with the katabatic wind forcing (inversion strength). Regime II represents the exceptional conditions at AWS 16 (Thiery et al., 2012; Gorodetskaya et al., 2013), where despite stable conditions and low wind speeds, SHF values are high probably due to large scale circulation effects. The model (Fig. 10b,c) does not simulate this regime accurately due to the limited spatial resolution as the station is positioned in a topographically complex region. Regime III represents the stable conditions of the AWSs in flat areas where static stability effects become important at high values of the temperature inversion, suppressing SHF.

For lower stabilities and towards summer conditions the branches join and SHF shows a linear dependence on T_{inv}, indicating the convective summertime conditions at plateau stations AWS 9 and 12 (Regime IV). This regime is exclusively found on the plateau, where the low summertime temperatures prevent sublimation (LHF) to act as a surface energy sink (King et al., 2006). Because

RACMO2 overestimates albedo and underestimates atmospheric transmissivity, a positive radiation balance is not simulated (at least not in the monthly mean sense) and convection does not occur.

Figure 10b, c shows the inability of RACMO2 to simulate regimes II and IV. The behaviour in the katabatic wind zone is represented well, although the branch is less pronounced due to the underestimation of the slope and hence wind speeds. RACMO2.3 simulates an improved separation of the most important regimes II and III compared to RACMO2.1, because of the improved surface layer turbulence scheme and general changes in the simulated results.

4 Conclusions

The physics package of the regional atmospheric climate model RACMO2 adopted from the ECMWF-IFS has been upgraded from cycle CY23r4 (RACMO2.1) to CY33r1 (RACMO2.3). This study evaluates the effects of this change on the surface energy balance (SEB), 10 m wind speed V_{10m} and surface temperature T_{s} by comparing both cycles with observational SEB data gathered from 9 automatic weather stations in East Antarctica and 64 deep snow temperature sites. The model has improved in several aspects. Due to the inclusion of a parameterization for cloud ice super-saturation, more clouds and increased moisture content are simulated in the upper troposphere. As a result, more clouds and an increased cloud optical thickness in the interior have resulted in more downward longwave radiation. Consequently, in RACMO2.3 the biases in the sensible heat flux (SHF) and the net longwave radiation (LW_{net}) have decreased from 10.4 to 6.3 $\mathrm{W\,m^{-2}}$ and -10.5 to $-7.1\,\mathrm{W\,m^{-2}}$, respectively. The change in longwave radiation has improved the bias in the SHF through its tight coupling with T_{s} and wind speed: the bias in T_{s}, based on the deep snow temperature observations, has decreased from -2.3 K to -1.3 K. Near-surface air temperatures have also increased but less so than T_{s}, decreasing the surface-based temperature inversion. The bias in V_{10m}, which is mainly due to the flattened ice sheet topography, remains unchanged.

Acknowledgements. We are grateful for the financial support of NWO/ALW, Netherlands Polar Programme. The installation and maintenance of AWS 16 was financed by the Belgian Science Policy Office under grant number EN/01/4B supervised by Nicole van Lipzig KU Leuven. We thank Irina Gorodetskaya for the use of the observational data.

References

Barker, H. W., Cole, J. N. S., Morcrette, J., and Pincus, R.: The Monte Carlo Independent Column Approximation : An assessment using several global atmospheric models, Quarterly Journal of the Royal Meteorological Society, 1478, 1463–1478, doi:10.1002/qj, 2008.

Beljaars, A. C., Brown, A. R., and Wood, N.: A new parametrization of turbulent orographic form drag, Quarterly Journal of the Royal Meteorological Society, 130, 1327–1347, doi:10.1256/qj.03.73, http://doi.wiley.com/10.1256/qj.03.73, 2004.

Chen, J. L., Wilson, C. R., Blankenship, D. D., and Tapley, B. D.: Antarctic mass rates from GRACE, Geophysical Research Letters, 33, L11 502, doi:10.1029/2006GL026369, http://www.agu.org/pubs/crossref/2006/2006GL026369.shtml, 2006.

Dee, D. P., Uppala, S. M., Simmons, A. J., Berrisford, P., Poli, P., Kobayashi, S., Andrae, U., Balmaseda, M. A., Balsamo, G., Bauer, P., Bechtold, P., Beljaars, A. C. M., Van de Berg, L., Bidlot, J., Bormann, N., Delsol, C., Dragani, R., Fuentes, M., Geer, A. J., Haimberger, L., Healy, S. B., Hersbach, H., Hólm, E. V., Isaksen, L., Kå llberg, P., Köhler, M., Matricardi, M., McNally, a. P., Monge-Sanz, B. M., Morcrette, J. J., Park, B. K., Peubey, C., de Rosnay, P., Tavolato, C., Thépaut, J. N., and Vitart, F.: The ERA-Interim reanalysis: configuration and performance of the data assimilation system, Quarterly Journal of the Royal Meteorological Society, 137, 553–597, doi:10.1002/qj.828, http://doi.wiley.com/10.1002/qj.828, 2011.

ECWMF-IFS: Part IV : Physical Processes (CY33R1), Tech. Rep. June, http://www.ecmwf.int/research/ifsdocs/CY33r1/PHYSICS/IFSPart4.pdf, 2008.

Ettema, J., Van den Broeke, M. R., Van Meijgaard, E., and Van de Berg, W. J.: Climate of the Greenland ice sheet using a high-resolution climate model Part 2: Near-surface climate and energy balance, The Cryosphere, 4, 529–544, doi:10.5194/tc-4-529-2010, http://www.the-cryosphere.net/4/529/2010/, 2010a.

Ettema, J., Van den Broeke, M. R., Van Meijgaard, E., Van de Berg, W. J., Box, J. E., and Steffen, K.: Climate of the Greenland ice sheet using a high-resolution climate model Part 1: Evaluation, The Cryosphere, 4, 511–527, doi:10.5194/tc-4-511-2010, http://www.the-cryosphere.net/4/511/2010/, 2010b.

Fettweis, X.: The Cryosphere Reconstruction of the 1979 - 2006 Greenland ice sheet surface mass balance using the regional climate model MAR, The Cryosphere, 1, 21–40, 2007.

Gorodetskaya, I. V., Van Lipzig, N. P. M., Van den Broeke, M. R., Mangold, A., Boot, W., and Reijmer, C. H.: Meteorological regimes and accumulation patterns at Utsteinen, Dronning Maud Land, East Antarctica: Analysis of two contrasting years, Journal of Geophysical Research, 118, 1–16, doi:10.1002/jgrd.50177, 2013.

Greuell, W. and Konzelmann, T.: Numerical modelling of the energy balance and the englacial temperature of the Greenland Ice Sheet. Calculations for the ETH-Camp location (West Greenland, 1155 m a.s.l.), Global and Planetary Change, 9, 91–114, doi:10.1016/0921-8181(94)90010-8, http://linkinghub.elsevier.com/retrieve/pii/0921818194900108, 1994.

King, J. C., Argentini, S. A., and Anderson, P. S.: Contrasts between the summertime surface energy balance and boundary layer structure at Dome C and Halley stations, Antarctica, Journal of Geophysical Research, 111, D02 105, doi:10.1029/2005JD006130, http://doi.wiley.com/10.1029/2005JD006130, 2006.

Kuipers Munneke, P., Van den Broeke, M. R., Lenaerts, J. T. M., Flanner, M. G., Gardner, A. S., and Van de Berg, W. J.: A new albedo parameterization for use in climate models over the Antarctic ice sheet, Journal

of Geophysical Research, 116, 1–10, doi:10.1029/2010JD015113, http://www.agu.org/pubs/crossref/2011/2010JD015113.shtml, 2011.

Lacis, A.: A Description of the Correlated k Distribution Method for Modeling Nongray Gaseous Absorption , Thermal Emission , and Multiple Scattering in Vertically Inhomogeneous Atmospheres to N2). Comparison cooling, Journal of Geophysical Research, 96, 9027–9063, 1991.

Lenaerts, J. T. M., Van den Broeke, M. R., Déry, S. J., Van Meijgaard, E., Van de Berg, W. J., Palm, S. P., and Sanz Rodrigo, J.: Modeling drifting snow in Antarctica with a regional climate model: 1. Methods and model evaluation, Journal of Geophysical Research, 117, 1–17, doi:10.1029/2011JD016145, http://www.agu.org/pubs/crossref/2012/2011JD016145.shtml, 2012.

Ligtenberg, S. R. M., Horwath, M., Van den Broeke, M. R., and Legrésy, B.: Quantifying the seasonal breathing of the Antarctic ice sheet, Geophysical Research Letters, 39, doi:10.1029/2012GL053628, http://doi.wiley.com/10.1029/2012GL053628, 2012.

Liu, H., Jezek, K., Li, B., and Zhao, Z.: Radarsat Antarctic Mapping Project digital elevation model version 2, Tech. rep., 2001.

Mlawer, E. J. and Clough, S. A.: Shortwave and Longwave Enhancements in the Rapid Radiative Transfer Model, in: Proc. 7th Atmospheric Radiation Measurement (ARM) Science Team Meeting, 1992, pp. 409–413, 1997.

Morcrette, J.-J., Barker, H. W., Cole, J. N. S., Iacono, M. J., and Pincus, R.: Impact of a New Radiation Package, McRad, in the ECMWF Integrated Forecasting System, Monthly Weather Review, 136, 4773–4798, doi:10.1175/2008MWR2363.1, http://journals.ametsoc.org/doi/abs/10.1175/2008MWR2363.1, 2008.

Reijmer, C. H. and Oerlemans, J.: Temporal and spatial variability of the surface energy balance in Dronning Maud Land, East Antarctica, Journal of Geophysical Research, 107, doi:10.1029/2000JD0001, 2002.

Reijmer, C. H., Van Meijgaard, E., and Van den Broeke, M. R.: Evaluation of temperature and wind over Antarctica in a Regional Atmospheric Climate Model using 1 year of automatic weather station data and upper air observations, Journal of Geophysical Research, 110, 1–12, doi:10.1029/2004JD005234, http://www.agu.org/pubs/crossref/2005/2004JD005234.shtml, 2005.

Rignot, E., Bamber, J. L., Van den Broeke, M. R., Davis, C., Li, Y., Van de Berg, W. J., and Van Meijgaard, E.: Recent Antarctic ice mass loss from radar interferometry and regional climate modelling, Nature Geoscience, 1, 106–110, doi:10.1038/ngeo102, http://www.nature.com/doifinder/10.1038/ngeo102, 2008.

Shepherd, A., Ivins, E. R., Geruo, A., Barletta, V. R., Bentley, M. J., Bettadpur, S., Briggs, K. H., Bromwich, D. H., Forsberg, R., Galin, N., Horwath, M., Jacobs, S., Joughin, I., King, M. A., Lenaerts, J. T. M., Li, J., Ligtenberg, S. R. M., Luckman, A., Luthcke, S. B., McMillan, M., Meister, R., Milne, G., Mouginot, J., Muir, A., Nicolas, J. P., Paden, J., Payne, A. J., Pritchard, H., Rignot, E., Rott, H., Sø rensen, L. S., Scambos, T. A., Scheuchl, B., Schrama, E. J. O., Smith, B., Sundal, A. V., Van Angelen, J. H., Van de Berg, W. J., Van den Broeke, M. R., Vaughan, D. G., Velicogna, I., Wahr, J., Whitehouse, P. L., Wingham, D. J., Yi, D., Young, D., and Zwally, H. J.: A Reconciled Estimate of Ice-Sheet Mass Balance, Science, 338, 1183–1189, doi:10.1126/science.1228102, http://www.sciencemag.org/content/338/6111/1183.abstract, 2012.

Siebesma, A. P., Soares, P. M. M., and Teixeira, J. a.: A Combined Eddy-Diffusivity Mass-Flux Approach for the Convective Boundary Layer, Journal of the Atmospheric Sciences, 64, 1230–1248, doi:10.1175/JAS3888.1, http://journals.ametsoc.org/doi/abs/10.1175/JAS3888.1, 2007.

Spichtinger, P., Gierens, K., and Read, W.: The global distribution of ice-supersaturated regions as seen by the Microwave Limb Sounder, Quarterly Journal of the Royal Meteorological Society, 129, 3391–3410, doi:10.1256/qj.02.141, http://doi.wiley.com/10.1256/qj.02.141, 2003.

Thiery, W., Gorodetskaya, I. V., Bintanja, R., Van Lipzig, N. P. M., Van den Broeke, M. R., Reijmer, C. H., and Kuipers Munneke, P.: Surface and snowdrift sublimation at Princess Elisabeth station, East Antarctica, The Cryosphere, 6, 841–857, doi:10.5194/tc-6-841-2012, http://www.the-cryosphere.net/6/841/2012/, 2012.

Tompkins, A. M. and Gierens, K.: Ice supersaturation in the ECMWF integrated forecast, Quarterly Journal of the Royal Meteorological Society, 133, 53–63, doi:10.1002/qj, 2007.

Turner, J., Colwell, S. R., Marshall, G. J., Lachlan-Cope, T. A., Carleton, A. M., Jones, P. D., and Reid, P. A.: The SCAR READER Project : Toward a High-Quality Database of Mean Antarctic Meteorological Observations, Journal of Climate, 17, 2890–2898, 2004.

Undén, P., Rontu, L., Jarvinen, H., Lynch, P., Calvo, J., Cats, G., Cuxart, J., Eerola, K., Fortelius, C., Garciamoya, J. A., Jones, C., Lenderlink, G., Mcdonald, A., Mcgrath, R., and Navascues, B.: HIRLAM-5 Scientific Documentation, Tech. Rep. December, Swedish Meteorology and Hydrology Institute, 2002.

Van de Berg, W. J., Van den Broeke, M. R., Reijmer, C. H., and Van Meijgaard, E.: Characteristics of the Antarctic surface mass balance, 1958-2002, using a regional atmospheric climate model, Annals of Glaciology, 41, 97–104, doi:10.3189/172756405781813302, http://openurl.ingenta.com/content/xref?genre=article\&issn=0260-3055\&volume=41\&issue=1\&spage=97, 2005.

Van de Berg, W. J., Van den Broeke, M. R., and Van Meijgaard, E.: Heat budget of the East Antarctic lower atmosphere derived from a regional atmospheric climate model, J. Geophys. Res., 112, D23 101, doi:10.1029/2007JD008613, 2007.

Van den Broeke, M. R.: Surface radiation balance in Antarctica as measured with automatic weather stations, Journal of Geophysical Research, 109, 1–17, doi:10.1029/2003JD004394, http://www.agu.org/pubs/crossref/2004/2003JD004394.shtml, 2004.

Van den Broeke, M. R.: Depth and density of the Antarctic firn layer, Arctic, Antarctic, and Alpine Research, 40, 432–438, doi:10.1657/1523-0430(07-021), http://instaar.metapress.com/index/q7667pg756287rw6.pdf, 2008.

Van den Broeke, M. R., Van As, D., Reijmer, C. H., and Van de Wal, R. S. W.: Assessing and Improving the Quality of Unattended Radiation Observations in Antarctica, Journal of Atmospheric and Oceanic Technology, 21, 1417–1431, doi:10.1175/1520-0426(2004)021⟨1417:AAITQO⟩2.0.CO;2, http://journals.ametsoc.org/doi/abs/10.1175/1520-0426(2004)021⟨1417:AAITQO⟩2.0.CO;2, 2004.

Van den Broeke, M. R., Reijmer, C. H., and Van As, D.: Seasonal cycles of Antarctic surface energy balance from automatic weather stations, Annals of Glaciology, 41, 131–139, http://www.ingentaconnect.com/content/igsoc/agl/2005/00000041/00000001/art00020, 2005a.

Van den Broeke, M. R., Van As, D., Reijmer, C. H., and Van de Wal, R. S. W.: Sensible heat exchange at the Antarctic snow surface: a study with automatic weather stations, International Journal of Climatology, 25, 1081–1101, doi:10.1002/joc.1152, http://doi.wiley.com/10.1002/joc.1152, 2005b.

Van Lipzig, N. P. M., Van Meijgaard, E., and Oerlemans, J.: The spatial and temporal variability of the surface mass balance in Antarctica: results from a regional atmospheric climate model, International Journal of Climatology, 22, 1197–1217, doi:10.1002/joc.798, http://doi.wiley.com/10.1002/joc.798, 2002.

Van Meijgaard, E., Van Ulft, L. H., Lenderink, G., De Roode, S. R., Wipfler, L., Boers, R., and Timmermans, A.: Refinement and application of a regional atmospheric model for climate scenario calculations of Western Europe, Climate changes Spatial Planning publication: KvR 054/12, 2012.

White, P. W.: Part IV : PHYSICAL PROCESSES (CY23R4), Tech. Rep. September, 2001.

Table 1. The AWS topographic characteristics and period of operation (until December 2011). Nr. months represents the number of available months over total months (725/770) of the model period (January 1979–December 2011). If no end time is indicated, the AWS is still operational end of 2011. Observed surface slope ($\mathrm{m\,km^{-1}}$) is based on a $1\mathrm{km} \times 1\mathrm{km}$ Digital Elevation Model (Liu et al., 2001), modelled surface slope is based on the 27 km interpolated grid.

AWS	4	5	6	8	9	10	11	12	16
Latitude	72°45′ S	73°06′ S	74°28′ S	76°00′ S	75°00′ S	79°34′ S	71°09′ S	78°39′ S	71°57′ S
Longitude	15°29.9′ W	13°09.9′ W	11°31.0′ W	08°03′ W	00°00′ E/W	45°47′ W	06°42′ W	35°38′ E	23°20′ E
Elevation (obs)	34 m	363 m	1160 m	2400 m	2892 m	890 m	700 m	3620 m	1300 m
Elevation (mod)	23 m	332 m	1219 m	2405 m	2856 m	789 m	224 m	3621 m	1130 m
Slope (obs)	1.0	23.1	38.4	2.0	1.5	1.1	15.5	2.0	15.6
Slope (mod)	3.4	7.8	28.9	3.5	2.0	5.1	10.7	2.2	16.2
Start	Dec 1997	Feb 1998	Jan 1998	Jan 1998	Dec 1997	Jan 2001	Jan 2007	Dec 2007	Feb 2009
End	Dec 2002	–	Jan 2009	Jan 2003	–	Jan 2006	–	–	–
nr. months	60/60	167/167	134/134	19/44	162/168	48/54	57/59	49/49	29/35

Table 2. Mean, bias (model – observation), standard deviation of the bias σ, root-mean-square deviation and correlation coefficient (r^2 with significance level $p < 0.0001$) for sensible heat flux (SHF), latent heat flux (LHF), net shortwave radiation (SW_{net}), net longwave radiation (LW_{net}), 10 m wind speed (V_{10m}) and surface temperature T_s as modelled by RACMO2.1 and RACMO2.3 and as observed with the 9 AWS's (770 months). Also shown are the values for annual averaged T_s in comparison with 10 meter snow temperatures from 64 ice core measurements. For calculation of the statistics all 770 months are used.

		Obs	RACMO2.1				RACMO2.3			
		mean	bias	σ_{bias}	RMSD	r^2	bias	σ_{bias}	RMSD	r^2
SHF	$[\mathrm{Wm^{-2}}]$	14.24	10.46	8.53	13.58	0.57	7.07	8.12	10.78	0.6
LHF	$[\mathrm{Wm^{-2}}]$	-2.11	0.56	2.95	3.0	0.31	0.36	2.77	2.79	0.38
$\mathrm{SW_{net}}$	$[\mathrm{Wm^{-2}}]$	22.73	-1.33	6.23	6.41	0.94	-1.96	7.60	7.86	0.92
$\mathrm{LW_{net}}$	$[\mathrm{Wm^{-2}}]$	-35.03	-10.36	9.83	14.22	0.66	-6.31	9.82	11.65	0.66
$\mathrm{V_{10m}}$	$[\mathrm{ms^{-1}}]$	6.38	-0.48	1.67	1.74	0.28	-0.51	1.64	1.72	0.27
$\mathrm{T_s(AWS)}$	[K]	244.28	-3.24	4.5	5.57	0.91	-1.91	4.36	4.77	0.91
T_s (ice cores)	[K]	240.6	-2.32	2.29	3.23	0.96	-1.28	2.13	2.45	0.98

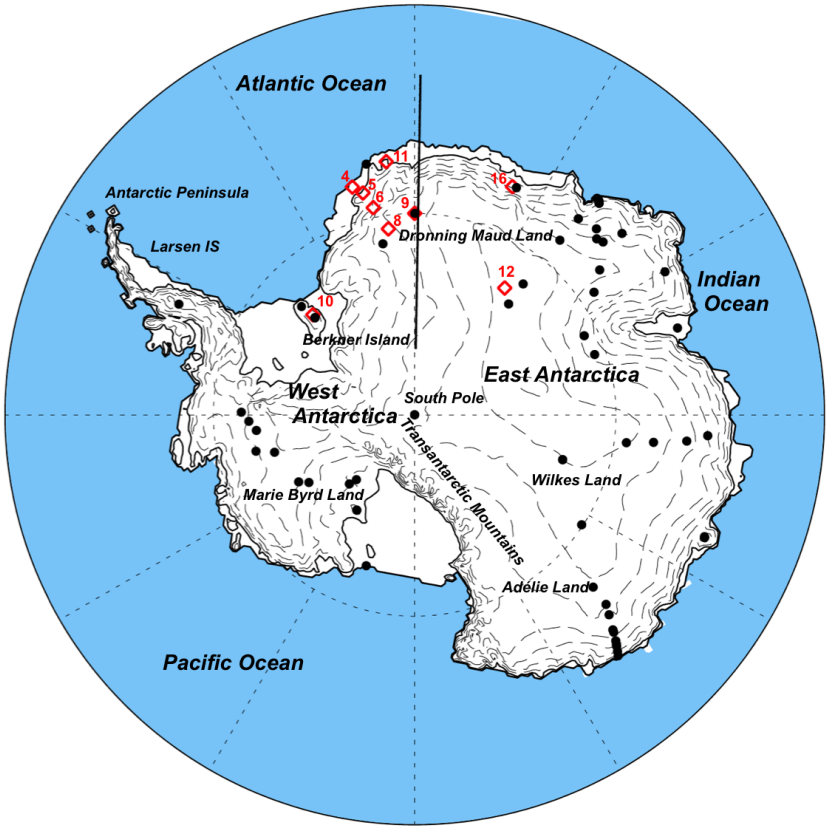

Fig. 1. Map of Antarctica with locations of the AWS (red diamonds) the 64 coring sites (black dots) and the position of the latitudinal cross-section used in Fig. 3. Also shown are the ice-shelf edge and grounding line (solid lines) and height intervals every 500 m (dashed lines) based on a digital elevation model from Liu et al. (2001).

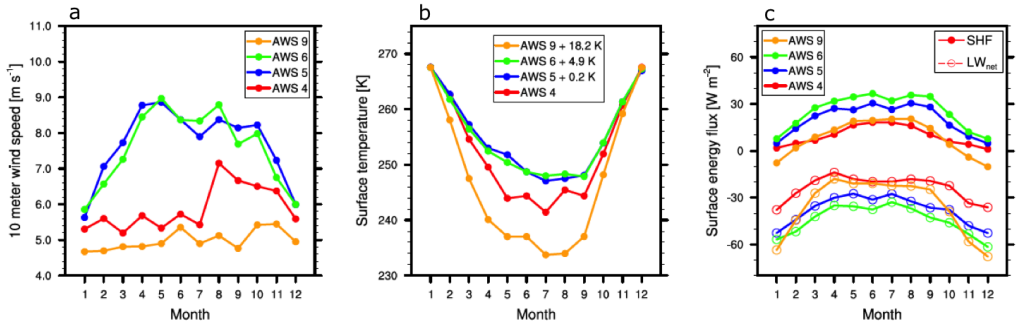

Fig. 2. Monthly mean **(a)** 10 m wind speed (V_{10m}), **(b)** surface temperature (T_s) and **(c)** sensible heat flux (SHF) and net longwave radiation (LW_{net}) for AWS 4, AWS 5, AWS 6 and AWS 9. The temperature curves for AWS 5, 6 and 9 (Fig. 2b) are shifted upward by 0.2, 4.9 and 18.2 K respectively, to correct for elevation and continentality differences (Van den Broeke, 2004).

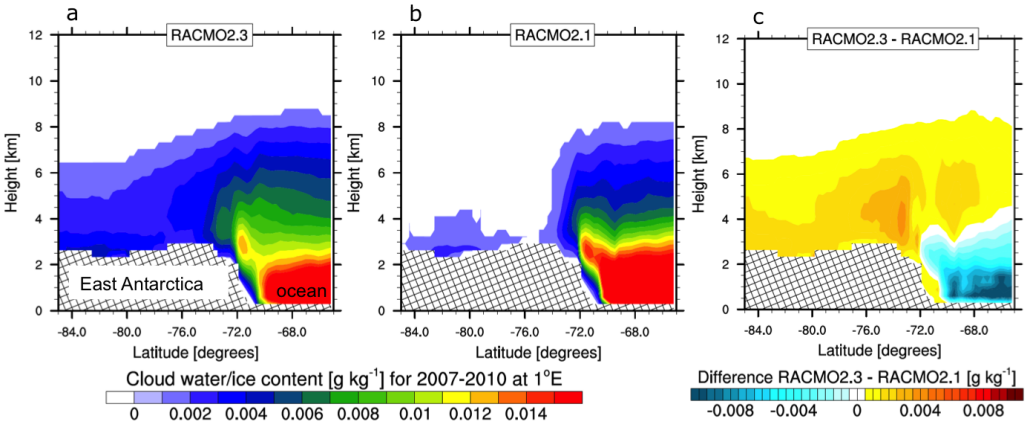

Fig. 3. Latitudinal cross-section of yearly (2007–2010) averaged total cloud water/ice content for **(a)** RACMO2.3, **(b)** RACMO2.1 and **(c)** the difference (RACMO2.3 – RACMO2.1) at 1° E. Location of cross-section is indicated in Fig. 1.

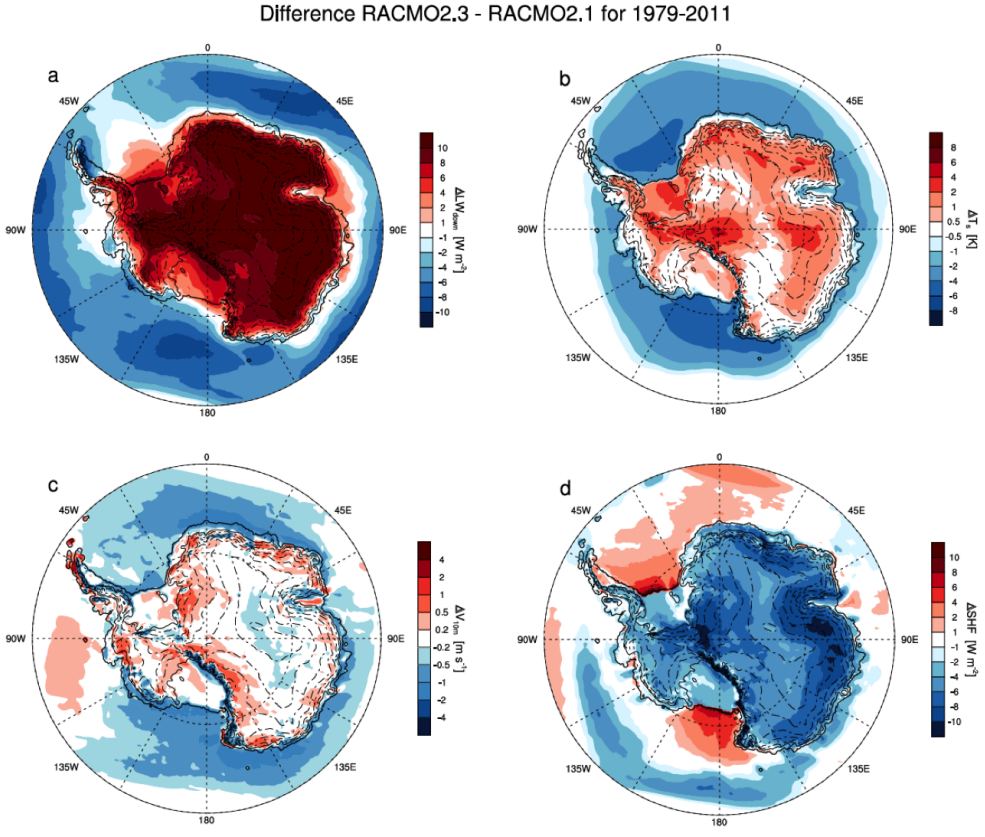

Fig. 4. Spatial distribution of difference (RACMO2.3 – RACMO2.1) for LW_{down} **(a)**, T_{s} **(b)**, V_{10m} **(c)** and SHF **(d)**.

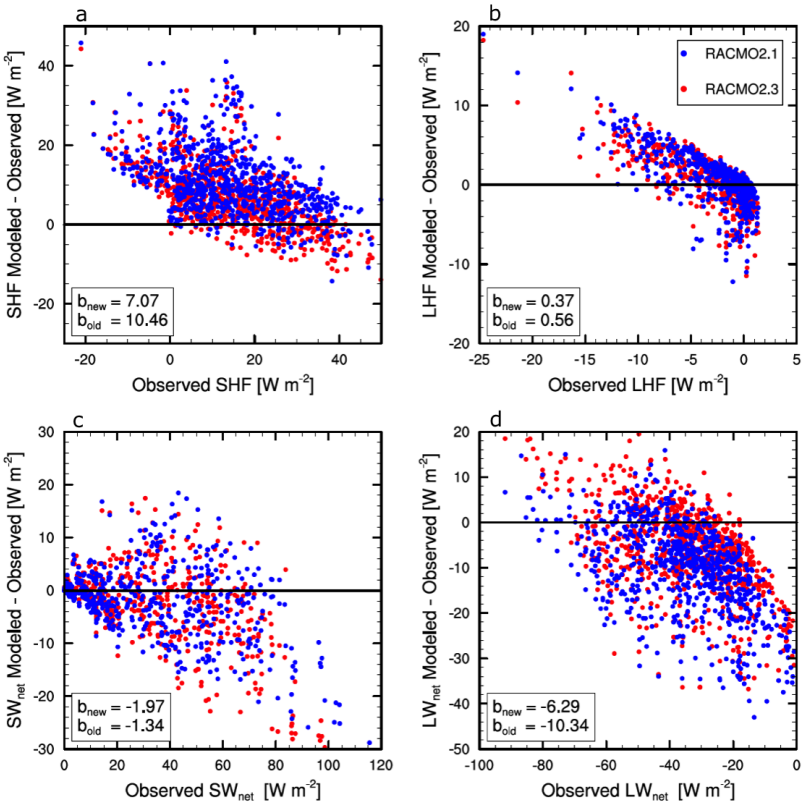

Fig. 5. Difference (modelled − observed) of **(a)** sensible heat flux (SHF), **(b)** latent heat flux (LHF), **(c)** net shortwave radiation (SW_{net}) and **(d)** net longwave radiation (LW_{net}) as a function of the AWS observations. Shown are RACMO2.3 (red) with bias b_{new} and RACMO2.1 (blue) with bias b_{old}. Biases (in [W m^{-2}]) are averages over all monthly average weather station data (> 750 data points).

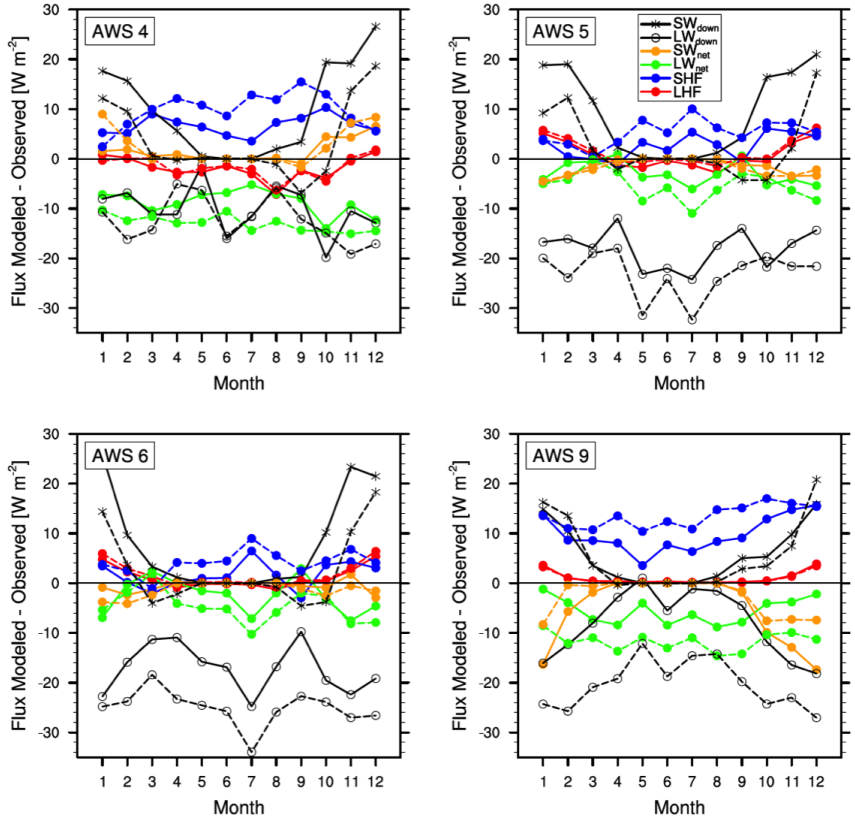

Fig. 6. Annual cycle of monthly mean difference (modelled – observed) of the SEB components (SHF (blue), LHF (red), SW_{net} (orange), LW_{net} (green)), LW↓ (black circles) and SW↓ (black asterisks) for **(a)** AWS 4, **(b)** AWS 5, **(c)** AWS 6 and **(d)** AWS 9. Shown are RACMO2.3 (solid line) and RACMO2.1 (dashed line).

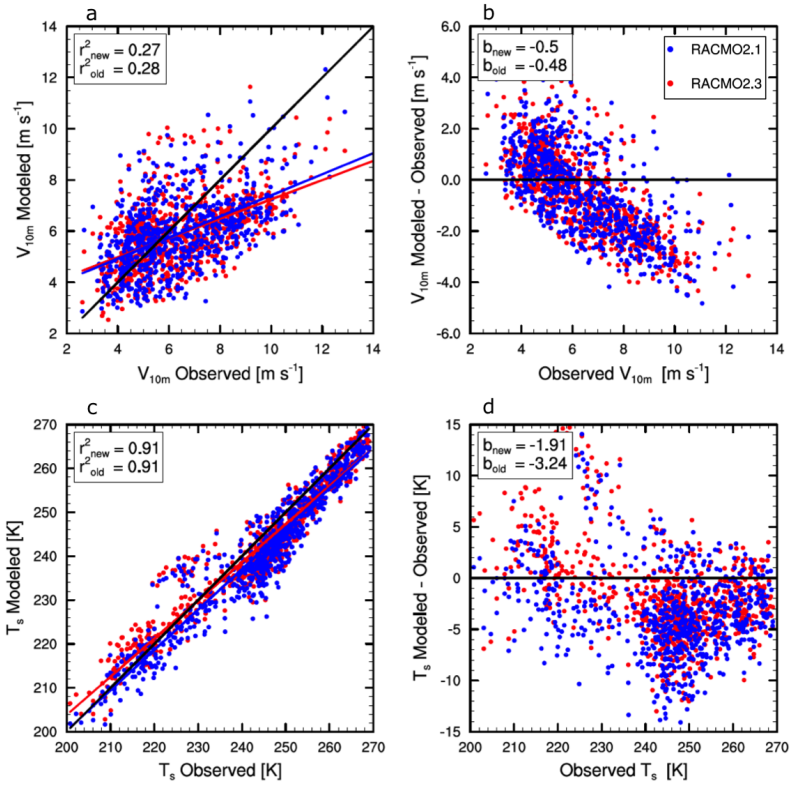

Fig. 7. Modelled and difference (modelled − observed) as a function of the AWS observations of **(a, b)** monthly averaged 10 m wind speed (V_{10m}) and **(c, d)** surface temperature (T_s). Shown are RACMO2.3 (red) with correlation r^2_{new} and bias b_{new} and RACMO2.1 (blue) with correlation r^2_{old} and bias b_{old}. Biases are averages over all data with units [m s^{-1}] for V_{10m} and [K] for T_s.

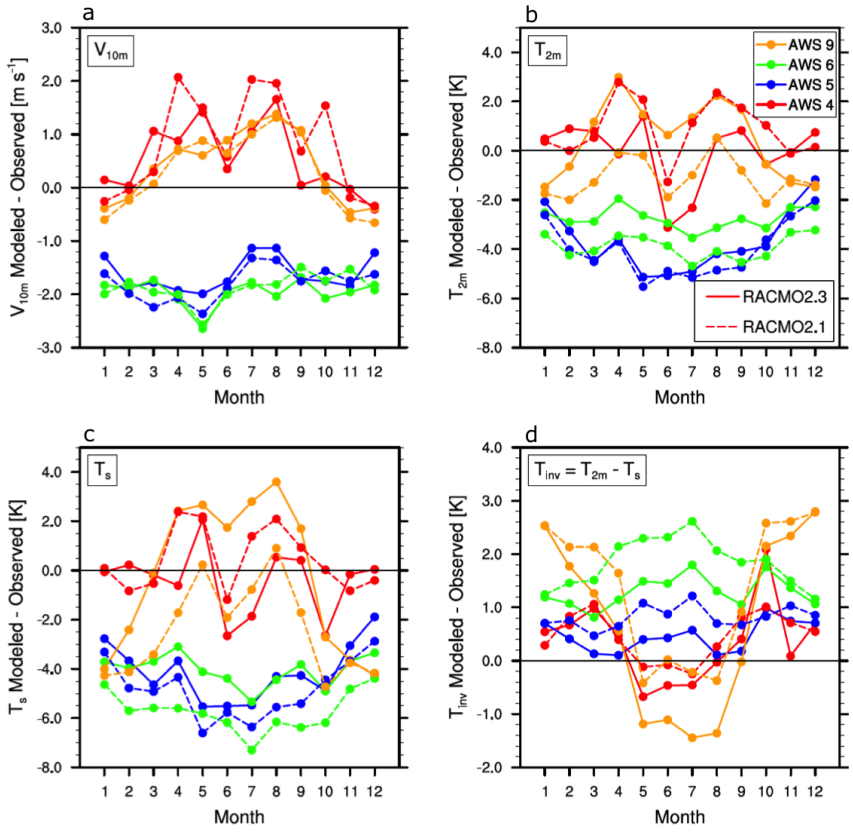

Fig. 8. Annual cycle of monthly mean difference (modelled − observed) of **(a)** 10 m wind speed (V_{10m}), **(b)** 2 m temperature (T_{2m}), **(c)** surface temperature ($T_{\rm s}$) and **(d)** the surface temperature inversion ($T_{inv} = T_{\rm 2m} - T_{\rm s}$) for AWS 4, AWS 5, AWS 6 and AWS 9. Shown are RACMO2.3 (solid line) and RACMO2.1 (dashed line).

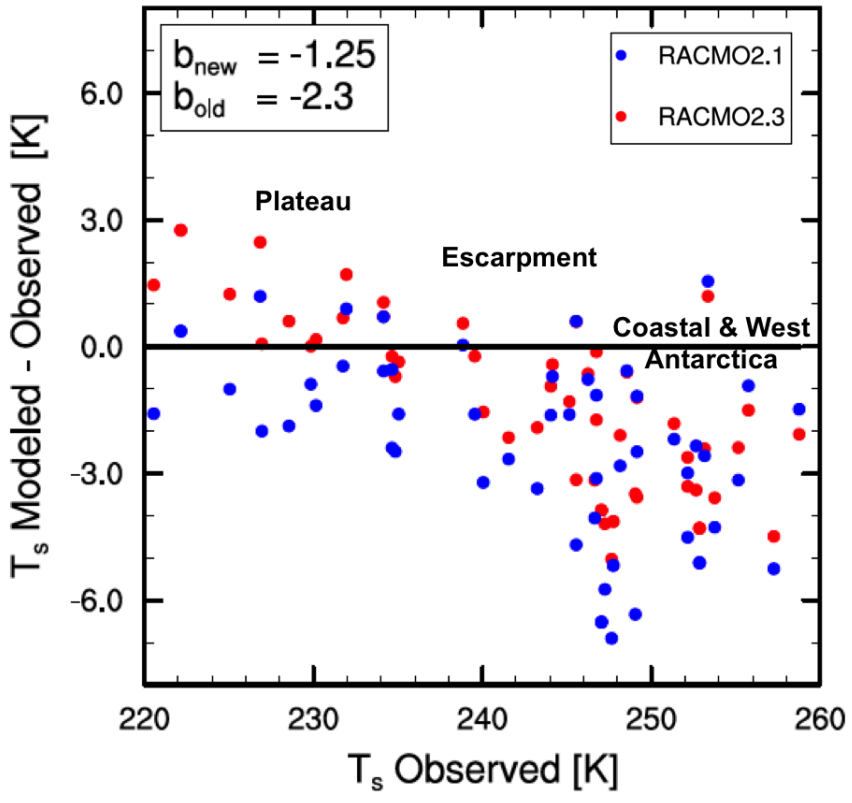

Fig. 9. Difference (modelled − observed) of the annual period averaged (1979–2011) surface temperature (T_s) as a function of 10 m ice core observations. Shown are RACMO2.3 (red) with bias b_{new} and RACMO2.1 (blue) with bias b_{old} (in [K]).

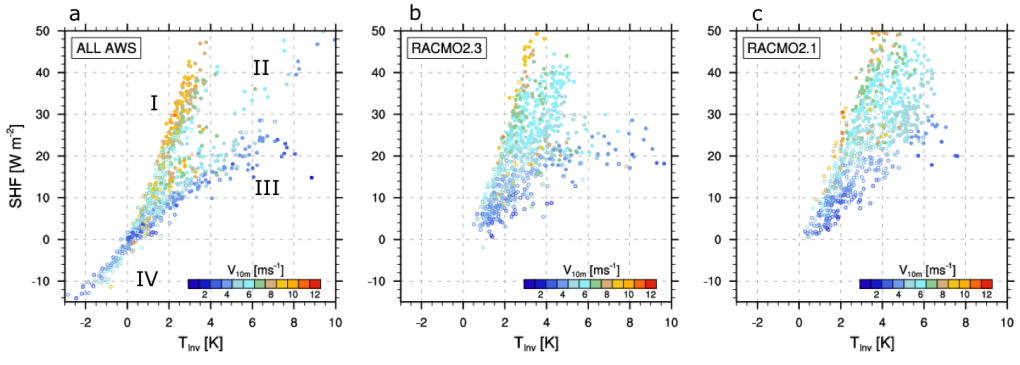

Fig. 10. Monthly averaged SHF as a function of the surface temperature inversion ($T_{inv} = T_{2\mathrm{m}} - T_\mathrm{s}$) for **(a)** all AWSs, **(b)** RACMO2.3 and **(c)** RACMO2.1. The color scheme represents wind speed V_{10m} and model data is from the same months and locations as the observational data. Filled circles are winter values (months 4–9) and open circles represent months (10–3). Four climate regimes are denoted, and explained in Sect. 3.5.